

FEMBA on the Edge: Physiologically-Aware Pre-Training, Quantization, and Deployment of a Bidirectional Mamba EEG Foundation Model on an Ultra-low Power Microcontroller

Anna Tegon, *Graduate Student Member, IEEE*, Nicholas Lehmann, Yawei Li, Andrea Cossetini, *Senior Member, IEEE*, Luca Benini, *Fellow, IEEE* and Thorir Mar Ingolfsson *Member, IEEE*

Abstract—Objective: To enable continuous, long-term neuro-monitoring on wearable devices by overcoming the computational bottlenecks of Transformer-based Electroencephalography (EEG) foundation models and the quantization challenges inherent to State-Space Models (SSMs). **Methods:** We present FEMBA, a bidirectional Mamba architecture pre-trained on over 21,000 hours of EEG. We introduce a novel Physiologically-Aware pre-training objective, consisting of a reconstruction with low-pass filtering, to prioritize neural oscillations over high-frequency artifacts. To address the activation outliers common in SSMs, we employ Quantization-Aware Training (QAT) to compress the model to 2-bit weights. The framework is deployed on a parallel ultra-low-power RISC-V microcontroller (GAP9) using a custom double-buffered memory streaming scheme. **Results:** The proposed low-pass pre-training improves downstream AUROC on TUAB from 0.863 to 0.893 and AUPR from 0.862 to 0.898 compared to the best contrastive baseline. QAT successfully compresses weights with negligible performance loss, whereas standard post-training quantization degrades accuracy by approximately 30%. The embedded implementation achieves deterministic real-time inference (1.70 s per 5 s window) and reduces the memory footprint by 74% (to ≈ 2 MB), achieving competitive accuracy with up to $27\times$ fewer FLOPs than Transformer benchmarks. **Conclusion:** FEMBA demonstrates that Mamba-based foundation models can be effectively quantized and deployed on extreme-edge hardware without sacrificing the representation quality required for robust clinical analysis. **Significance:** This work establishes the first full-stack framework for deploying large-scale EEG foundation models on ultra-low-power wearables, facilitating continuous, SSM based monitoring for epilepsy and sleep disorders.

Index Terms—Electroencephalography, Foundation Models, Mamba, Quantization, Edge AI, Wearables, RISC-V.

I. INTRODUCTION

Electroencephalography (EEG) measures cortical electrical activity using non-invasive electrodes. Since its earliest use in the 1920s, EEG has become a fundamental tool for monitoring brain activity [1], with clinical applications spanning the diagnosis of sleep disorders, neurodegenerative diseases, and epilepsy [2], [3].

In recent years, EEG applications have been moving outside controlled clinical environments. Clinically, there is a need for continuous, long-term monitoring in ambulatory and at-home settings, for example in the context of epilepsy monitoring [4]. At the same time, the consumer market shows increased interest towards wellness-oriented brain monitoring solutions and brain computer interfaces (BCI), with applications spanning aided meditation, boosting productivity, and gaming [5], [6].

This project was supported by the Swiss National Science Foundation (Project PEDESITE) under grant agreement 193813. This work was also supported in part by the ETH Future Computing Laboratory (EFCL) and by a grant from the Swiss National Supercomputing Centre (CSCS) under project ID lp12 on Alps.

Anna Tegon, Nicolas Lehmann, Yawei Li, Andrea Cossetini, Luca Benini, and Thorir Mar Ingolfsson are with the Integrated Systems Laboratory, ETH Zürich, Zürich, Switzerland (thoriri@iis.ee.ethz.ch).

Luca Benini is also with the DEI, University of Bologna, Bologna, Italy.

As EEG expands beyond controlled clinical environments, there is a pressing need to enable continuous monitoring and on-device EEG signal analysis on resource-constrained wearable devices. Such systems must operate under tight computational and power constraints [7], while being more susceptible to movement and environmental artifacts affecting signal quality [8], [9].

In this context, the algorithmic landscape for EEG analysis is rapidly evolving. Classical EEG analysis initially relied on hand-crafted spectral, temporal, or spatial features combined with traditional classifiers such as Support Vector Machines, Linear Discriminant Analysis, and tree-based methods [10].

Overcoming the limitations of manual feature engineering prompted a shift toward end-to-end learning, with convolutional neural networks [11] enabling automatic feature extraction and improved decoding performance. Despite the increased memory and computational demands, there have been multiple demonstrations of model deployments on edge devices for low-power execution on wearables [12]–[14]. However, existing approaches still struggle to generalize across subjects, recording platforms, and electrode configurations, often requiring task-specific and patient-specific data collections and training.

Foundation Models (FMs) address the generalization limitations of deep learning by pre-training on large-scale, unlabeled EEG corpora and adapting to downstream tasks through transfer learning. Recent models such as BENDR [15], LaBraM [16], and CbraMod [17] demonstrate improved cross-subject generalization and reduced annotation requirements. However, while FMs offer the robust generalization capabilities required for diverse patient populations, their reliance on Transformer architectures with quadratic complexity $\mathcal{O}(N^2)$ renders them computationally prohibitive for wearable devices. This disconnect prevents the deployment of state-of-the-art AI on the very edge devices required for long-term, continuous neuro-monitoring.

State-space models (SSMs), such as Mamba [18], offer a promising avenue to avoid the fundamental quadratic complexity bottleneck, by reformulating sequence modeling as a latent dynamical system with linear scaling $\mathcal{O}(N)$ in sequence length. Yet, two critical barriers remain for their adoption in biomedical edge computing. First, standard self-supervised pre-training objectives (e.g., masked reconstruction) often force models to reconstruct high-frequency artifacts (e.g., EMG noise), wasting model capacity on non-physiologically meaningful characteristics of the raw signals. Second, Mamba architectures are notoriously difficult to quantize due to activation outliers, so naive integer post-training quantization can lead to severe performance collapse on low-precision microcontrollers (MCUs).

Building on our previous FEMBA architecture [19], which introduced a bidirectional Mamba-based EEG foundation encoder, we present an end-to-end framework that bridges the gap between large-scale FMs and ultra-low-power wearable hardware. Our specific contributions are in addition to open-sourcing our code and models for reproducibility¹:

¹<https://github.com/pulp-bio/BioFoundation>

- **Physiologically-Aware Pre-training:** We introduce a self-supervised objective, *Reconstruction with Low-pass Filtering*, that acts as a denoising autoencoder by forcing the encoder to reconstruct a low-pass-filtered target instead of raw EEG. On Temple University Abnormal Corpus (TUAB), this objective improves Area Under the Receiver Operating Characteristic (AUROC) from 0.863 to 0.893 and Area Under the Precision-Recall (AUPR) from 0.862 to 0.898 compared to the best contrastive baseline, with significant accuracy improvement (78.6% \rightarrow 81.9%). On Temple University Artifact Corpus (TUAR) and Temple University Slowing Corpus (TUSL), performance differences between the pre-training strategies are within overlapping confidence intervals. The low-pass variant remains competitive and does not compromise performance on these smaller datasets, while consistently avoiding the degradation observed with contrastive masking.
- **Robust Mamba Quantization:** We systematically study post-training quantization (PTQ) and show that activation outliers in Mamba-style SSMs make naive W8A8 PTQ collapse performance (AUROC 0.89 \rightarrow 0.77, accuracy 81% \rightarrow 55%), and that W2A8 PTQ fails completely. By switching to Quantization-Aware Training (QAT), we recover near-floating-point performance for W8A8 and W4A8 (within \approx 0.01 AUROC of FP32) and even for W2A8². This yields a 2-bit-weight, 8-bit-activation FEMBA-Tiny variant that is both accurate and deployable on tightly constrained MCUs where standard PTQ fails.
- **Full-Stack Edge Deployment:** We demonstrate, to the best of our knowledge, the first deployment of a SSM-based EEG foundation model on a parallel ultra-low-power RISC-V MCU. Using optimized kernels and a double-buffered multi-level memory streaming scheme, we achieve deterministic inference of a 5 s window in **1.70 s** at 370 MHz, at an energy cost of **75 mJ per inference**, at an average power envelope of 44.1 mW, while compressing the model footprint from 7.8 MB (INT8) to \sim 2 MB (2-bit weights). This shows that foundation-scale EEG encoders can be made compatible with the memory and latency budgets of continuous MCU-based, wearable monitoring devices.

These three components—physiologically-aware pre-training, robust quantization, and full-stack deployment—are tightly coupled. The low-pass reconstruction objective stabilizes the encoder’s frequency content, which in turn simplifies the quantization landscape. The resulting quantized model is architected to match the memory hierarchy and processing architecture of MCUs.

Compared to our preliminary FEMBA paper [19], which introduced the original bidirectional Mamba encoder and demonstrated the feasibility of pre-training and fine-tuning on TUAB, TUAR, and TUSL, this work makes three key extensions. First, we systematically compare four self-supervised objectives and propose a physiologically-aware low-pass reconstruction target that significantly improves downstream performance on TUAB. Second, we present, to our knowledge, the first comprehensive quantization study of Mamba for EEG, showing that quantization-aware training enables a W2A8 configuration that remains competitive with full-precision baselines. Third, we develop a full-stack deployment framework targeting a low-power MCU, including custom kernels, hierarchical streaming, and a detailed cycle-accurate analysis, demonstrating that FEMBA can meet the memory and latency of MCU’s highly constrained compute and storage.

II. RELATED WORK

²while activation 4-bit quantization remains unstable in our experiments

A. Supervised Deep Learning for EEG

Early applications of supervised deep learning to EEG primarily relied on convolutional neural networks (CNNs). An important early contribution was the DeepConvNet and ShallowConvNet [20] architectures, which showed that end-to-end CNNs operating directly on raw EEG could match the performance of traditional feature-engineering pipelines. Building on these ideas, EEGNet [21] introduced a more compact and efficient CNN design based on depthwise-separable convolutions, better capturing the spatiotemporal structure of EEG while remaining lightweight and portable. Numerous variants and derived models emerged, including MBEEGNet [22], TIDNet [23] and related architectures, which extend its capabilities through temporal modules, multi-scale processing, and attention mechanisms. In parallel to CNN-based models, recurrent architectures were explored to better capture the temporal dynamics of EEG signals. Early examples include LSTM-based classifiers [24], which demonstrated that sequence models applied to sliding windows of raw EEG can effectively learn temporal dependencies, and RNN frameworks combined with sliding-window CSP features [25], which highlighted the potential of recurrent networks for modeling temporal structure in motor-imagery decoding.

B. Foundation Models for EEG Analysis

Recent foundation models for EEG increasingly rely on self-supervised learning (SSL) to exploit large-scale unlabeled recordings. Early work such as BENDR [15] adapted masked prediction frameworks by combining convolutional encoders with contrastive objectives to reconstruct masked EEG representations. Later approaches extended this paradigm using Transformer-based architectures: BrainBERT [26] performs masked prediction on channel-independent spectrograms for iEEG, while models such as LaBraM [16] apply vector-quantized masking and discrete latent spaces to learn robust codebooks. Recent developments, as CBraMod [17], reconstruct masked raw signal patches directly, enabling end-to-end learning of temporal and spatial EEG structure.

However, a common limitation across these approaches is their agnostic treatment of frequency content. By attempting to reconstruct the full spectral bandwidth, which includes high-frequency noise and muscle artifacts [9], these models may allocate capacity to modeling non-physiological interference rather than cortical dynamics. This suggests an opportunity for physiologically-aware pre-training objectives that prioritize neural oscillations over broadband reconstruction.

Despite the progress of Transformer-based foundation models, their quadratic time and memory complexity with respect to sequence length ($\mathcal{O}(n^2)$) limits their practicality in many real-world EEG scenarios, especially in wearable or edge-computing settings where compute and memory resources are constrained [13]. Applications such as continuous epilepsy monitoring further impose real-time requirements and strict false-alarm tolerances [9].

State-space model (SSM) architectures offer a compelling alternative, as their linear complexity ($\mathcal{O}(N)$) enables efficient processing of long sequences, and recent designs, such as Mamba [18], demonstrate strong sequence-modeling performance. While Mamba-based EEG models have begun to emerge—such as EEGMamba [27] and EEGM2 [28], which employ Mixture-of-Experts and U-Net architectures, respectively—these works focus primarily on algorithmic performance on high-end GPUs, leaving the challenges of edge deployment and quantization largely unexplored.

C. Efficient Edge AI and Quantization Challenges

EEG processing is commonly performed offline or on high-performance hardware, and existing surveys mainly focus on acquisition and usability rather than embedded computation. A few recent

works started to explore edge-based EEG processing, showing that lightweight CNNs can run on MCUs, though with strict constraints on memory and latency [29]. Due to these limitations, several studies have investigated model compression—including pruning, quantization, and compact architectures—to enable deployment on low-power devices [13].

However, deploying Foundation Models (specifically SSMs) presents unique challenges compared to standard CNNs. While CNNs are often robust to low-bit quantization (e.g., 8-bit or 4-bit), Mamba architectures are notoriously difficult to quantize. Recent studies in computer vision [30] highlight that Mamba’s selective scan mechanism generates activation outliers that destroy performance under standard Post-Training Quantization (PTQ). Consequently, bridging the gap between Mamba’s theoretical efficiency and actual hardware implementation requires dedicated Quantization-Aware Training (QAT) strategies that have not yet been applied to the EEG domain.

D. Limitations of Prior Works

In this context, prior works demonstrated the growing interest in self-supervised EEG representation learning, yet they reveal clear limitations. As shown in Table I, existing foundation models rely on Transformer architectures with quadratic complexity, translating to computational costs up to $27\times$ higher than linear alternatives. Simultaneously, many EEG applications, from Brain-Computer Interfaces to continuous ambulatory monitoring, require online inference on low-power wearable devices. However, the development of foundation models and edge-AI solutions has largely progressed in isolation: as shown in Table I, **none of these models report edge deployment**, leaving the gap between algorithmic performance and embedded feasibility unaddressed. While state-space models such as Mamba [18] offer linear complexity, their deployment on ultra-low-power devices remains unexplored in the biomedical literature.

We address these gaps by deploying a bidirectional Mamba foundation model for biosignal analysis running on an ultra-low-power edge MCU.

TABLE I: Comparison of EEG foundation models

Model	Architecture	Size	Datasets	Complexity	Deployment
EEGFormer	Transformer	2.3M	TUAR / TUSL	$\mathcal{O}(CN^2)$	No
LaBraM	Transformer	5.9M	TUAB	$\mathcal{O}(C^2N^2)$	No
LUNA	Transformer	7M	TUAB / TUAR / TUSL	$\mathcal{O}(CN^2) + \mathcal{O}(CN)$	No
FEMBA	Mamba-based	7.8M	TUAB / TUAR / TUSL	$\mathcal{O}(CN)$	Yes

C number of EEG channels
 N number of temporal patches

III. METHODS

A. Datasets

We leveraged the Temple University EEG Corpus (TUEG) [31] for pretraining, as it is one of the largest publicly available clinical EEG repositories. The corpus contains over 21,600 hours of recordings from more than 14,000 patients. The TUEG dataset includes several labeled subsets designed for specific diagnostic tasks. The **TUAB** subset provides recordings labeled as normal or abnormal (binary classification) for 2,329 subjects. The **TUAR** comprises data from 213 subjects and, following prior work [19], we treat it as a multiclass (single-label) classification task with five classes corresponding to five artifact types. The **TUSL** includes recordings from 38 subjects for the detection and classification of slowing events, seizures, complex backgrounds, and normal EEG activity [31] (multiclass classification).

TABLE II: Dataset Statistics

Property	TUEG	TUAB	TUAR	TUSL
Number of Subjects	14,987	2,329	213	38
Number of Channels	22	22	22	22
Sampling Rate	256 Hz	256 Hz	256 Hz	256 Hz
Hours of Recordings	21,787.32	1,139.31	83.74	27.54
Training Samples	13,236,000	591,357	49,241	16,088
Validation Samples	489,600	154,938	5,870	1,203
Test Samples	489,600	74,010	5,179	2,540

B. Preprocessing

We applied a standard pre-processing pipeline to the raw EEG recordings. All signals were band-pass filtered between 1 Hz and 75 Hz, and a 60 Hz notch filter was used to remove power line interference. Signals were then resampled to 256 Hz for consistency across recordings. After resampling, each raw signal was segmented into non-overlapping 5 s windows for training and evaluation.

An initial analysis of the TUEG dataset showed that most signals (about 96%) were within the range of $-20.16\mu\text{V}$ to $19.96\mu\text{V}$, while the remaining recordings contained values with much higher magnitudes. To preserve dataset integrity and ensure comparability with prior work using the full TUEG dataset, we retained all recordings, including those with extreme values. Given x , raw EEG signal, x_{norm} corresponds to its normalized version, which is then provided as input to the model. To reduce the influence of these artifacts during training, we applied quartile-based normalization [32], scaling each channel by its interquartile range (IQR):

$$x_{\text{norm}} = \frac{x - q_{\text{lower}}}{(q_{\text{upper}} - q_{\text{lower}}) + 1 \times 10^{-8}}$$

where q_{lower} and q_{upper} denote the 25th and 75th percentiles (i.e., the lower and upper quartiles) of each channel’s amplitude distribution, respectively. The small constant 1×10^{-8} is added for numerical stability.

C. Model Architecture

We build on the architecture introduced in our previous work [19]. With the goal of enabling model deployment on low-power MCUs, we adopt the *FEMBA-Tiny* configuration for all the following experiments. The Tiny variant consists of a 2D convolutional tokenizer that projects the raw EEG input into an embedding space of dimension $d_{\text{model}} = 385$. The encoder is composed of two Bidirectional Mamba (Bi-Mamba) blocks, which process the sequence in both forward and backward directions to capture complex temporal dependencies. A residual connection is included within each Bi-Mamba block to support gradient flow during training.

A key architectural novelty is the introduction of an additional lightweight Transformer layer in the decoder. Specifically, we integrate this layer to enhance the model’s contextual reasoning capabilities. This hybrid design leverages the structured state-space modeling of Mamba with the contextual reasoning ability of self-attention [33]. The decoder is used only during pretraining and is discarded in downstream classification, preserving the linear computational complexity of the model during fine-tuning.

In the classification stage, a simple linear classifier is employed, consisting of a single fully connected layer. This minimalistic task-specific output layer highlights the key role of the pretrained encoder.

D. Pre-training

Recent work on foundational EEG models has explored a range of pretraining strategies, showing promise for both masked-reconstruction approaches [17] and contrastive learning methods [15].

In this study, we aim to investigate whether one pretraining paradigm consistently yields stronger performance. To this end, we evaluate four pretraining techniques: two based on contrastive learning and two based on masked reconstruction.

We pretrain FEMBA-Tiny on the TUEG dataset (see Sect. III-A). All subjects and recordings contained in the downstream datasets (TUAB, TUAR, and TUSL) were excluded from the pretraining to ensure a fair assessment of the model’s generalization capabilities.

1) Masked Reconstruction Approaches: In these setups, the input signal is divided into 80 non-overlapping patches of size 16. A random subset of these patches is replaced with a fixed mask token using a masking ratio between 0.5 and 0.6, consistent with prior work [16]. The model is trained to reconstruct the original signal $\hat{x} = f(x_m)$ by minimizing the Smooth L1 loss [34]:

$$\text{SmoothL1}(\hat{x}, x) = \begin{cases} 0.5(x - \hat{x})^2/\beta, & \text{if } |x - \hat{x}| < \beta, \\ |x - \hat{x}| - 0.5\beta, & \text{otherwise.} \end{cases} \quad (1)$$

We compute the loss over all patches, weighting unmasked patches by 0.1 to maintain consistent representations. We evaluate two specific reconstruction targets:

a) Low-pass Filtering: While high-frequency components (e.g., HFOs) contain relevant biomarkers, they are frequently contaminated by muscle artifacts (Electromyography (EMG)) in scalp EEG [9]. For robust ambulatory monitoring, we prioritize low-frequency morphology (0.5–40 Hz) [35]. We apply a 2nd-order biquad low-pass filter (40 Hz cutoff) to the *target* signal only. This introduces an implicit denoising objective, encouraging the model to recover meaningful neural activity while ignoring the high-frequency noise.

b) Clustered Random Patches: To increase reconstruction task difficulty, we employ a clustered masking strategy. Instead of independent random masking, we group masked regions into contiguous segments, maintaining the 0.5 to 0.6 ratio. This prevents the model from relying on local interpolation and forces it to learn longer-range relations, temporal structure, and cross-channel dependencies.

2) Contrastive Learning Approaches: We also evaluate contrastive learning, which aims to learn discriminative representations by pulling together positive pairs (augmented views of the same signal) and pushing away negative pairs [36]. We maximize the similarity between views using the standard InfoNCE loss [37]:

$$\mathcal{L}_{\text{InfoNCE}} = -\log \frac{\exp(\text{sim}(z_i, z_i^+)/\tau)}{\sum_{j=1}^N \exp(\text{sim}(z_i, z_j)/\tau)}, \quad (2)$$

where z_i and z_i^+ are embeddings of two views of the same signal, and τ is the temperature parameter. We explore two view-generation strategies:

a) Frequency-domain Augmentations: Following Rommel *et al.* [38], we make views using three complementary transformations which simulate inter-subject variability and sensor noise: (1) *FT Surrogate* [39], which randomizes phase while preserving the magnitude spectrum; (2) *Frequency Shift* [40], which shifts spectral components via the Hilbert transform; and (3) additive Gaussian noise.

b) Masking-based Augmentations: Inspired by self-supervised audio learning [41], we generate positive pairs by applying two non-overlapping binary masks to the same input signal. Unlike reconstruction, which focuses on waveform details, this objective forces the model to identify latent neural patterns that are semantically consistent across different temporal views of the recording.

E. Fine-tuning Methodology

We evaluated **FEMBA-Tiny** on EEG-based classification tasks, specifically three downstream tasks: *epilepsy detection* (TUAB), *slowing event detection* (TUSL), and *artifact detection* (TUAR).

We maintained the same downstream tasks as in our prior work [19], as they provide a broad spectrum of classification scenarios, including both binary and multi-class settings. Moreover, these tasks span different application domains, from clinical diagnostics to artifact identification, requiring the model to adapt to diverse signal characteristics. For TUAB, we preserved the standard train-test partition provided with the dataset. For TUSL and TUAR, which lack predefined subject-level splits, we followed the evaluation protocol established by recent state-of-the-art methods, including EEGFormer [42], applying a randomized 80%/10%/10% division at the sample level for training, validation, and testing to ensure fair and direct comparison with existing benchmark results. For TUAR specifically, we formulated the problem as a 5-class single-label classification task, focusing on five distinct artifact categories, consistent with prior work.

For the classifier architecture, we removed the decoder and replaced it with a lightweight linear classification head. Thanks to the improvements introduced during pretraining, we were able to eliminate the additional Mamba block used in the previous setup. This change reduced the number of parameters in the classification head from approximately 0.7 million to just a few thousand, significantly simplifying the fine-tuning process.

For the TUAB dataset, which is relatively balanced, we adopted the standard cross-entropy loss, as it consistently yields stable and robust training performance. Conversely, for the imbalanced TUAR and TUSL datasets, we employed the Focal Loss [43] to mitigate class imbalance. The loss function is defined as:

$$\text{FL}(p_t) = -\alpha_t(1 - p_t)^\gamma \log(p_t) \quad (3)$$

where p_t denotes the predicted probability of the correct class, α_t is a class-balancing factor, and γ is a focusing parameter. Focal Loss reduces the impact of well-classified samples and emphasizes harder, minority-class examples, while rebalancing each class contribution by frequency. This approach proved particularly effective for the TUSL dataset, which exhibits significant class imbalance.

We performed fine-tuning using the AdamW optimizer with a batch size of 256 over 50 epochs. The learning rate was set to 5e-4 with a layer-wise learning rate decay of 0.7. Additionally, we applied a weight decay of 0.05 and a gradient clipping threshold of 1.0, while dropout was set to 0.0.

F. Quantization

To quantize FEMBA-Tiny, we utilized *Brevitas*, a PyTorch-based library for neural network quantization that supports both Post-Training Quantization (PTQ) and Quantization Aware Training (QAT) [44]. These represent the two general approaches to quantization, depending on when quantization is applied. PTQ is performed after training, while QAT is conducted during training [45].

PTQ is the simplest approach for quantizing a pre-trained model. It typically relies on basic assumptions and statistics to perform the quantization. This process can be improved through *calibration*, which in *Brevitas* is implemented using the `calibration_mode` and `bias_correction_mode` functions. These allow collecting activation statistics in floating point with quantization temporarily disabled, and then re-enabling quantization with properly initialized scales, followed by optional bias correction.

On the other hand, QAT is the most complex yet effective quantization method, as it simulates quantization during training, allowing the model to adapt to quantization effects and reduce accuracy degradation.

In our evaluation of FEMBA-Tiny, we quantized both weights and activations down to 2-bit precision. We use **per-channel uniform**

quantization for the weights. For each output channel c , a separate scale factor $s_w^{(c)}$ is learned. The quantization process is given by:

$$q_w^{(c)} = \text{round}\left(\frac{w^{(c)}}{s_w^{(c)}}\right), \quad \hat{w}^{(c)} = s_w^{(c)} \cdot q_w^{(c)},$$

where $w^{(c)}$ denotes the original weights in channel c , $s_w^{(c)}$ is the per-channel floating-point scale, $q_w^{(c)}$ is the quantized integer representation, and $\hat{w}^{(c)}$ is the reconstructed (dequantized) weight.

For activations, instead of using a floating-point scale, we opted for a more hardware-friendly fixed-point quantization by constraining the scale to be a power-of-two value:

$$s_a = 2^{-n}, \quad q_a = \text{round}\left(\frac{a}{s_a}\right), \quad \hat{a} = s_a \cdot q_a,$$

where a is the original activation value, s_a is the power-of-two scale, q_a is the quantized activation, and \hat{a} is the reconstructed activation.

This design choice enables efficient implementation on hardware accelerators by replacing multiplication with bit-shifting operations.

G. Embedded deployment

We deploy the quantized FEMBA-Tiny model on the GAP9 RISC-V MCU [46] to demonstrate for the first time the feasibility of running Mamba-based foundation models on extreme edge devices.

1) **Hardware and Memory Hierarchy:** The GAP9 features a cluster of 9 RISC-V cores (8 workers, 1 orchestrator) with a hierarchical memory architecture: 128 kB L1 scratchpad, 1.5 MB shared L2, and off-chip L3 HyperRAM [47]. We utilize the XpulpV2 ISA extensions, including a 4-way INT8 SIMD dot-product and hardware loops, to accelerate compute-intensive operations.

To handle weights exceeding on-chip capacity, we implemented a **hierarchical double-buffered streaming strategy**. Large weight matrices are partitioned into ≈ 80 kB chunks and streamed L3 \rightarrow L2 via DMA. Simultaneously, the cluster orchestrator manages L2 \rightarrow L1 tiling, prefetching weights into L1 double-buffers while worker cores compute on the current tile. This hides memory latency and enables deployment of models limited only by external storage size.

2) **Hybrid Quantization and Kernels:** We employ a **hybrid quantization strategy** tailored to the numerical requirements of SSMs. We developed a custom toolchain to export parameters directly from Brevitas to optimized C kernels.

a) **Linear Projections (INT8):** The input/output projections and gate generations dominate the parameter count. We quantize these to INT8 and parallelize execution across the 8 worker cores. The kernels use an output stationary dataflow with 4×4 loop unrolling (over outputs and timesteps) to maximize register reuse. The innermost loop utilizes SIMD instructions to perform four MACs per cycle, accumulating into an INT32 to prevent overflow.

b) **Selective SSM Scan (Q15):** The recurrent scan $h_t = \bar{A} \cdot h_{t-1} + \bar{B} \cdot x_t$ is sensitive to quantization noise. We implement this operation using Q15 fixed-point arithmetic (15-bit fractional precision). Unlike the linear layers, the scan contains sequential temporal dependencies, preventing time-dimension parallelization. Instead, we adopt a **channel-parallel strategy**: the $d_{inner} = 1540$ channels are distributed across cores, with each core processing its subset sequentially over time. To also avoid expensive runtime floating-point exponentials, the discretizations parameters (\bar{A} , \bar{B}) and SiLU activations are precomputed using Lookup Tables (LUTs).

3) **Deployment Toolchain:** We developed a custom code generation pipeline to deploy FEMBA-Tiny on GAP9. The pipeline extracts quantized weights and activation scales directly from the Brevitas-trained PyTorch model [44], bypassing ONNX to maintain precise control over quantization parameters. A template-based C code generator produces layer-specific kernels with tiling configurations optimized for GAP9’s memory hierarchy. The Mamba-specific operators (selective scan, gating, bidirectional combination) are implemented as custom kernels integrated into the GAP SDK build system. This approach enables bit-exact reproducibility between the Python reference implementation and the embedded deployment [48].

IV. RESULTS

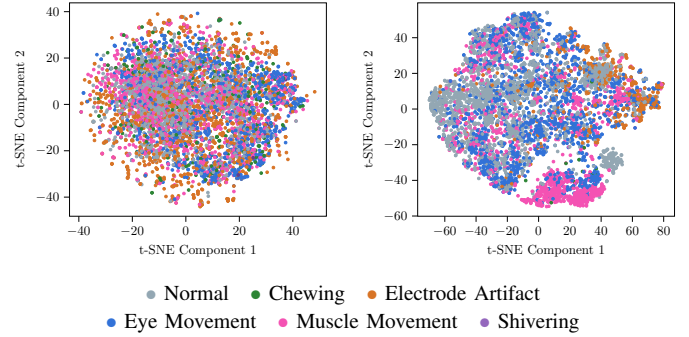


Fig. 1: t-SNE visualization of embedding spaces on downstream tasks. **Left:** Embeddings generated using the earlier training pipeline show lower class separability. **Right:** Embeddings obtained with the updated pipeline yield tighter, more distinct clusters for artifact classes (e.g., muscle movement), illustrating an improvement in the learned representation quality.

A. Pre-training Performance-Comparisons

To identify the optimal pre-training objective, we compared the four proposed strategies across the TUAB, TUAR, and TUSL datasets, as summarized in Table III.

For the smaller TUAR and TUSL datasets, the differences between pre-training strategies are modest and fall within overlapping confidence intervals, precluding claims of a superior method.

In contrast, the larger TUAB dataset reveals distinct performance hierarchies. The **Reconstruction–Random with LowPass** strategy emerges as the superior approach, outperforming all alternatives across every metric. Most notably, it achieves a $>3.5\%$ improvement in AUROC compared to the *Contrastive–Frequency* baseline and maintains a $\sim 2\%$ lead in AUPR against all other methods. In terms of accuracy, it remains competitive with the *Clustered Random* variant while surpassing the contrastive approaches by margins of 1–3%.

Having established *Reconstruction–Random with LowPass* as the most effective pretraining strategy for FEMBA, we also compared the resulting encoder with the previous version of the model [19]. Since the decoder is discarded during fine-tuning, the downstream performance depends entirely on the quality of the learned representations. As illustrated qualitatively in Fig. 1, the new pipeline produces embeddings that form more coherent class-specific clusters (e.g., distinguishing muscle artifacts from eye movements), indicating a substantial improvement in representation quality.

B. Fine-tuning Performance

Given the considerations discussed in Section IV-A, we adopt the *Reconstruction–Random with LowPass* configuration as the new

TABLE III: Comparison of Fine-tuning Results Across TUAR, TUSL, and TUAB Datasets for Different Pre-training Strategies

SSL Task	TUAR		TUSL		TUAB		
	AUROC	AUPRC	AUROC	AUPRC	Accuracy (%)	AUROC	AUPRC
Rec. – Random Masking	0.912 ± 0.002	0.532 ± 0.011	0.699 ± 0.028	0.281 ± 0.019	80.38 ± 0.08	0.8762 ± 0.0012	0.8773 ± 0.0011
Rec. – Clustered Random	0.917 ± 0.004	0.547 ± 0.027	0.712 ± 0.023	0.281 ± 0.019	81.38 ± 0.09	0.8663 ± 0.001	0.8654 ± 0.0011
Rec. – Random w/ Lowpass	0.916 ± 0.008	0.533 ± 0.024	0.750 ± 0.035	0.294 ± 0.009	81.95 ± 0.09	0.8930 ± 0.0007	0.8976 ± 0.0018
Contrastive – Frequency	0.921 ± 0.007	0.534 ± 0.023	0.751 ± 0.020	0.291 ± 0.014	78.63 ± 0.09	0.8633 ± 0.0007	0.8615 ± 0.0015
Contrastive – Masking	0.915 ± 0.012	0.533 ± 0.014	0.695 ± 0.020	0.272 ± 0.004	80.69 ± 0.07	0.8732 ± 0.0006	0.8691 ± 0.0007

pretraining strategy for all downstream tasks. In Tables IV and V, we report results for all downstream evaluations and compare them with the smallest available architecture of the original FEMBA model for each respective dataset, as well as to recent state-of-the-art (SoA) EEG foundation models. Since the new FEMBA architecture is fine-tuned using the smallest possible classifier (a linear head), whereas the original FEMBA required a heavy Mamba classifier, we ensure fairness by comparing the new FEMBA model against the original pretrained FEMBA encoder fine-tuned with both a Mamba classifier and a linear classifier.

1) *TUAB dataset*: Compared to the smallest model previously used (FEMBA-Base [19]), the updated FEMBA demonstrates improved performance when evaluated against both variants of the original model, i.e., the version fine-tuned with the Mamba classifier and the version fine-tuned with a linear classifier.

With respect to the **Mamba-classifier** baseline, we observe slightly higher accuracy (around 1%) and AUPR (around 1%), while obtaining similar AUROC values. When comparing against the **Linear-classifier** version of the original model, gains are more substantial: approximately 2% in accuracy, 4% in AUROC, and up to 5% in AUPR, despite having roughly 6× fewer parameters.

Overall, the new FEMBA ranks among the strongest models on the benchmark. It is analogous to LaBraM-Base [16], performing marginally better in accuracy (around a 0.5% improvement) while showing minimally worse AUROC and AUPR (around 0.5%). Compared to much larger models such as LaBraM-Huge and CBraMod [17], the accuracy drop remains modest (only 0.5–0.6%), despite their massively larger parameter counts, highlighting the efficiency of the proposed 7.8M-parameter architecture.

Notably, this improved performance is achieved with only 1.3G FLOPs, up to 6× fewer than FEMBA Base and 27× fewer than LaBraM-Base.

2) *TUAR dataset*: Among the previous FEMBA variants, the smallest directly comparable model is FEMBA-Tiny. When comparing the updated FEMBA to the original Tiny model fine-tuned with the **Mamba-classifier**, the two models exhibit equivalent AUROC performance, as their confidence intervals nearly overlap, while the updated version achieves a modest improvement in AUPR (about 2% on average). Against the Tiny model fine-tuned with a **Linear-classifier**, the updated FEMBA shows clearer gains: AUROC improves by roughly 2–3%, and AUPR by nearly 6%, despite operating at essentially the same parameter scale. In comparison to state-of-the-art models, the updated FEMBA achieves competitive performance. Compared to the much larger LUNA-Huge [49] (SoA AUROC), it achieves slightly higher average AUPR (on the order of 0.5%), while exhibiting AUROC confidence intervals that closely overlap, thus reaching comparable results with approximately 40× fewer parameters. When compared to the larger FEMBA-Base (SoA AUC-PR), the updated model reaches similar AUROC values while showing lower AUPR (around 2–3%). Overall, these results demonstrate that the updated FEMBA achieves a favorable trade-off between model size and performance across both metrics.

3) *TUSL dataset*: On the TUSL dataset, as shown in Table IV, the updated FEMBA demonstrates consistent improvements over previous models of comparable size. Relative to the original Tiny model (the smallest version of the previous FEMBA) equipped with the **Mamba-classifier**, AUROC and AUPR increase by approximately 4% and 1.5%, respectively. A comparison with the **Linear-classifier** variant reveals even larger gains in AUROC, around 5%, while the improvement in AUPR remains similar to the previous case. When benchmarked against leading models, the updated FEMBA maintains a competitive standing. Although LUNA-Huge (SOTA AUROC) surpasses it by roughly 5–6% in AUROC, their AUPR scores are nearly indistinguishable, with overlapping confidence intervals, despite FEMBA using approximately 40× fewer parameters. Compared to EEGFormer-Base (SOTA AUPR), the updated model attains a higher AUROC (≈ 3–4%), but lags in AUPR by approximately 10%.

TABLE IV: Comparison of model performance on TUAR and TUSL datasets.

Model	Size	TUAR		TUSL	
		AUROC †	AUC-PR †	AUROC †	AUC-PR †
<i>Supervised Models</i>					
EEGNet [21]	-	0.752 ± 0.006	0.433 ± 0.025	0.635 ± 0.015	0.351 ± 0.006
EEG-GNN [50]	-	0.837 ± 0.022	0.488 ± 0.015	0.721 ± 0.009	0.381 ± 0.004
GraphS4mer [51]	-	0.833 ± 0.006	0.461 ± 0.024	0.632 ± 0.017	0.359 ± 0.001
<i>Self-supervised Models</i>					
BrainBERT [26]	43.2M	0.753 ± 0.012	0.350 ± 0.014	0.588 ± 0.013	0.352 ± 0.003
EEGFormer-Base [42]	2.3M	0.847 ± 0.014	0.483 ± 0.026	0.713 ± 0.010	0.393 ± 0.003
EEGFormer-Large [42]	3.2M	0.852 ± 0.004	0.483 ± 0.014	0.679 ± 0.013	0.389 ± 0.003
FEMBA-Base [19]	47.7M	0.900 ± 0.010	0.559 ± 0.002	0.731 ± 0.012	0.289 ± 0.009
FEMBA-Large [19]	77.8M	0.915 ± 0.003	0.521 ± 0.001	0.714 ± 0.007	0.282 ± 0.010
LUNA-Base [49]	7M	0.902 ± 0.011	0.495 ± 0.010	0.767 ± 0.023	0.301 ± 0.003
LUNA-Huge	311.4M	0.921 ± 0.011	0.528 ± 0.012	0.802 ± 0.005	0.289 ± 0.008
FEMBA old - Mamba classifier [19]	8.5M*	0.918 ± 0.003	0.518 ± 0.002	0.708 ± 0.005	0.277 ± 0.007
FEMBA old - Linear classifier	7.8M*	0.893 ± 0.021	0.475 ± 0.025	0.688 ± 0.030	0.272 ± 0.007
FEMBA new - Linear classifier	7.8M*	0.916 ± 0.008	0.533 ± 0.024	0.750 ± 0.035	0.294 ± 0.009

* Model size including the classification head

† Bold indicates state-of-the-art models under 10M parameters.

TABLE V: Performance comparison on TUAB abnormal EEG detection.

Model	Size	Bal. Acc. (%) †	AUC-PR †	AUROC †
<i>Supervised Models</i>				
SPARCNet [52]	0.8M	78.96 ± 0.18	0.8414 ± 0.0018	0.8676 ± 0.0012
ContraWR [53]	1.6M	77.46 ± 0.41	0.8421 ± 0.0140	0.8456 ± 0.0074
CNN-Transformer [54]	3.2M	77.77 ± 0.22	0.8433 ± 0.0039	0.8461 ± 0.0013
FFCL [55]	2.4M	78.48 ± 0.38	0.8448 ± 0.0065	0.8569 ± 0.0051
ST-Transformer [56]	3.2M	79.66 ± 0.23	0.8521 ± 0.0026	0.8707 ± 0.0019
<i>Self-supervised Models</i>				
BENDR [15]	0.39M	76.96 ± 3.98	-	0.8397 ± 0.0344
BrainBERT [26]	43.2M	-	0.8460 ± 0.0030	0.8530 ± 0.0020
EEGFormer-Base [42]	2.3M	-	0.8670 ± 0.0020	0.8670 ± 0.0030
BIOT [57]	3.2M	79.59 ± 0.57	0.8692 ± 0.0023	0.8815 ± 0.0043
EEG2Rep [58]	-	80.52 ± 2.22	-	0.8843 ± 0.0309
CEREBRO [59]	85.15M	81.67 ± 0.23	0.9049 ± 0.0026	0.8916 ± 0.0038
LaBraM-Base [16]	5.9M	81.40 ± 0.19	0.8965 ± 0.0016	0.9022 ± 0.0009
LaBraM-Huge [16]	369.8M	82.58 ± 0.11	0.9204 ± 0.0011	0.9162 ± 0.0019
CBraMod [17]	69.3M	82.49 ± 0.25	0.9221 ± 0.0015	0.9136 ± 0.0017
FEMBA old - Mamba classifier [19]	48.3M*	81.05 ± 0.14	0.8894 ± 0.0050	0.8829 ± 0.0021
FEMBA old - Linear classifier	47.6M*	79.75 ± 0.15	0.8511 ± 0.0011	0.8456 ± 0.0011
FEMBA new - Linear classifier	7.8M*	81.95 ± 0.09	0.8930 ± 0.0007	0.8976 ± 0.0018

* Model size including the classification head

† Bold indicates state-of-the-art models under 10M parameters.

C. Quantization Analysis

We focus our quantization analysis on TUAB, being the most extensively explored dataset in the literature [60]. TUAB also offers a controlled evaluation setting thanks to its balanced binary classification task, which allows us to isolate the effects of quantization more reliably. Table VI summarizes the quantization results.

We first evaluated the behavior of the model quantizing only the weights to 8-bit, 4-bit, and 2-bit. The 8-bit as well as 4-bit quantization resulted in negligible performance degradation (0.1% AUROC for 8-bit and 0.1% for both AUROC and AUPR for 4-bit). However, reducing to 2-bit led to a substantial degradation in accuracy, AUROC and AUPR. Quantizing activations, even at 8-bit precision, yielded an accuracy drop of approximately 30%, resulting in performance comparable to random guessing (accuracy ≈ 0.5). We extensively explored PTQ calibration pipelines in an attempt to mitigate this degradation. Following the procedure detailed in Section III-F, we performed activation calibration in floating point with quantization temporarily disabled, using a dedicated calibration split constructed to be class-balanced and representative of both seizure and non-seizure windows. We experimented with calibration sets ranging from approximately 5% to 20% of the TUAB training windows, confirming that neither increasing the calibration set size nor enforcing class balance produced any measurable improvement. After collecting activation statistics, we re-enabled quantization with the calibrated scales and applied bias correction, yet performance remained essentially unchanged.

This persistent failure of PTQ aligns with recent analyses of Mamba and other state-space models, which report that these architectures naturally generate large activation outliers, particularly in gate and output projections and their associated matrix multiplications. The parallel scan operation further amplifies these effects, resulting in heavy-tailed activation distributions that are inherently difficult to capture with low-precision quantization [30]. Given the relatively small model size, we were able to apply QAT. After a few epochs, QAT recovered the original AUROC, AUPR, and accuracy for weight-only 8-bit and for weight 4-bit with 8-bit activations. Even in the 2-bit weight and 8-bit activation setting, despite the significant drop with PTQ in AUROC and AUPR, QAT effectively restored performance, reaching results comparable to those obtained for weight 8-bit or weight 4-bit. However, when quantizing activations to 4-bit, QAT was not sufficient to recover performance.

TABLE VI: Quantization Results: Comparison of PTQ and QAT Performance

Configuration	Method	AUROC	AUPR	Accuracy
FP32 (Baseline)	–	0.89	0.89	81.84
W8A8	PTQ	0.77	0.71	55.91
	QAT	0.88	0.88	81.02
W4A8	PTQ	0.71	0.67	55.79
	QAT	0.88	0.88	80.88
W2A8	PTQ	0.56	0.49	54.12
	QAT	0.88	0.88	80.61
W4A4	PTQ	0.68	0.63	54.95
	QAT	0.69	0.68	65.40
W2A4	PTQ	0.54	0.54	48.38
	QAT	0.55	0.55	49.20
Only Weight 8	PTQ	0.88	0.89	81.61
Only Weight 4	PTQ	0.88	0.88	80.86
Only Weight 2	PTQ	0.54	0.48	54.71

In the remainder of this work we therefore focus on a QAT-trained *FEMBA-Tiny* model with a W2A8 configuration for the encoder weights and activations, combined with a small number of higher-precision accumulators where required for numerical stability. On GAP9, this scheme primarily reduces the model’s memory footprint,

from 7.8 MB for a uniform INT8 implementation to approximately 2 MB, while leaving the runtime dominated by the sequential SSM scan. We use the corresponding W8A8 model as our on-device INT8 baseline. In other words, quantization is crucial to make *FEMBA-Tiny* fit within the L3/L2 memory budgets of the device and to enable efficient streaming, whereas further reductions in latency will require architectural changes to the SSM itself rather than more aggressive bitwidth scaling. In the next subsection, we deploy both the W8A8 and W2A8 *FEMBA-Tiny* models on GAP9 and characterize their end-to-end latency, energy, and cycle breakdown.

D. Model deployment on a low-power microcontroller

We now evaluate the QAT-trained *FEMBA-Tiny* models on a GAP9-based ultra-low-power MCU platform. In particular, we compare the uniform INT8 (W8A8) baseline against the 2-bit weight variant (W2A8) selected in the quantization analysis and quantify the impact of 2-bit weights on latency, energy, and memory footprint. As discussed above, both models share the same network architecture and differ only in the numerical representation of the encoder weights and the associated packing/unpacking logic; all activations remain 8-bit on device.

1) *Experimental Setup:* We evaluated *FEMBA-Tiny* on a GAP9 development board [9], [46] with the compute cluster operating at 370 MHz. Performance measurements use the GAP9 hardware performance counters to obtain cycle-accurate timing and instruction counts. Each inference processes a 5 s input window with 22 channels and 1,280 timesteps (256 Hz sampling), represented as a tensor of shape (22, 1280), with embedding dimension $d_{model} = 385$. All reported metrics are averaged over 10 runs with identical inputs to ensure measurement stability. MACs/cycle values refer to dense-equivalent INT8 multiply-accumulate operations.

Table VII summarizes the end-to-end execution metrics for the standard INT8 implementation and the 2-bit weight quantization variant.

2) *Latency and Efficiency:* The INT8 deployment achieves an inference latency of 1.70 seconds for a 5-second input window (629.4 million cycles), which in turn yields a real-time slack factor of approximately 3x. At the measured average power of 44.1 mW, this corresponds to an energy cost of 75 mJ per 5 s inference window (1.70 s of active compute). At the TUSL sampling rate this corresponds to roughly 3 \times faster-than-real-time processing, leaving ample slack for on-device pre- and post-processing. Our double-buffered streaming architecture successfully hides nearly all memory transfer latency, achieving 99.4–100% overlap between computation and L3 \rightarrow L2 DMA transfers in the Mamba blocks.

To put these numbers into a more practical perspective, for a typical 300 mAh, 3.7 V wearable battery (around 4.0 kJ of stored energy), this energy cost would allow on the order of 5.3×10^4 such 5 s inference windows, corresponding to roughly 3 days of continuous operation for *FEMBA* inference alone, ignoring the additional overhead of sensing, storage, and wireless communication. While a full device-level power budget is beyond the scope of this work, these estimates suggest that *foundation-scale EEG encoders can be integrated into wearable neuro-monitoring systems without violating typical battery and form-factor constraints.*

As Table VIII shows, the two bidirectional Mamba blocks account for 98.3% of total cycles, while other layers, patch embedding, positional encoding, global pooling, and classification contribute negligibly to latency. This concentration of runtime in the Mamba blocks confirms that they are the primary target for further optimization.

3) *Sub-operation Analysis and Efficiency:* To localize bottlenecks within the Mamba blocks, we instrumented each sub-

operation. Table IX reports the breakdown for the first Mamba block (`mamba_blocks.0`).

a) *Memory Bandwidth Saturation*: Our hierarchical memory management strategy proves highly effective for the compute-intensive layers. The Input and Output Projections achieve high computational density, reaching 2.65 and 3.91 MACs/cycle, respectively. This performance confirms that our multi-level double-buffered tiling successfully eliminates memory bandwidth bottlenecks: despite the Input Projection requiring the streaming of 1.13 MB of weights from off-chip L3 memory, the DMA/Compute overlap remains >99%, ensuring that the cores are never stalled waiting for data.

b) *Shift from MACs/Cycle to IPC*: In contrast, the Selective SSM Scan dominates execution time (64.6% of cycles) while contributing only a small fraction of the total MACs. This discrepancy highlights a critical distinction for deploying State Space Models: unlike CNNs or Transformers, where performance scales with arithmetic throughput (MACs/cycle), *efficiency in Mamba-based models is defined by Instructions per Cycle (IPC)*

To validate this, we analyzed hardware performance counters. The SSM scan achieves a high **IPC of 1.36**, indicating that the GAP9 dual-issue pipeline is fully utilized. However, the recurrence inherently requires approximately **4.3 supporting instructions** (pointer arithmetic, LUT-based parameter discretization, and state management) per MAC operation. Therefore, low MAC utilization in the SSM scan is not a sign of inefficiency, but a characteristic of the algorithm. We conclude that future hardware-software optimization for SSMs must pivot away from maximizing MAC density and instead toward handling complex, scalar instruction streams at high IPC.

4) *Impact of 2-bit Quantization*: We compared the INT8 baseline against 2-bit weight quantization (Table VII). While 2-bit quantization reduces the model storage by 74% (≈ 2 MB vs. 7.8 MB), end-to-end latency remains nearly unchanged (1.69 s vs. 1.70 s).

The 2-bit weights are packed four values per byte using a ternary encoding ($\{-1, 0, +1\} \mapsto \{0, 1, 2\}$), yielding 16 weights per 32-bit word. During inference, weights are unpacked on the fly within the dot-product loop: each iteration extracts four 2-bit values via shift-and-mask operations, maps them back to $\{-1, 0, +1\}$ as INT8, and feeds them to the same SIMD dot-product instructions used by the INT8 kernel. This adds roughly eight simple ALU operations per eight weights, which is negligible compared to the memory-access and accumulation costs, explaining why latency is nearly unchanged despite the $4\times$ reduction in weight memory traffic [48], [61]. This behavior is consistent with prior work on PULP-class MCUs, where sub-byte quantization mainly improves model size and energy efficiency, while 8-bit SIMD remains throughput-optimal in the absence of dedicated low-bit instructions [48], [61].

These results confirm that FEMBA-Tiny is compute-bound rather than memory-bound on GAP9. The 2-bit variant is therefore primarily beneficial for reducing external-memory energy and storage footprint on resource-constrained wearables.

5) *Accuracy*: The embedded implementation achieves bit-exact consistency with the Python simulation. We validated the output of every layer, confirming a bit-to-bit exact implementation for both the INT8 and 2-bit configurations.

V. DISCUSSION

A. Physiological Awareness in Foundation Models

Our results demonstrate that the *Reconstruction–Random with LowPass* strategy significantly outperforms standard masking and contrastive approaches. We hypothesize that this objective functions as a domain-specific regularizer. Standard masked modeling forces the network to allocate capacity to reconstructing high-frequency

TABLE VII: FEMBA-Tiny Performance on GAP9 @ 370 MHz

Metric	INT8 (W8A8)	2-bit (W2A8)
Total Cycles	629.4 M	625.9 M
Inference Time	1.70 s	1.69 s
Compute Utilization	98.6%	98.7%
Idle/Overhead	0.5%	0.5%
DMA/Compute Overlap	99.4%	99.5%

TABLE VIII: Layer-by-Layer Cycle Breakdown

Layer	Cycles (M)	% Total	Overlap
patch_embed	8.0	1.3%	81.1%
pos_embed	2.3	0.4%	100.0%
mamba_blocks.0	310.3	49.3%	100.0%
mamba_blocks.1	308.2	49.0%	99.4%
global_pool	0.5	0.1%	100.0%
classifier	<0.1	<0.01%	41.9%
Total	629.4	100%	—

components, which in scalp EEG are often dominated by electromyographic (EMG) artifacts and environmental noise [62]. By filtering the reconstruction target, we explicitly direct the model’s attention toward the delta–beta bands (0.5–30 Hz), which contain the majority of clinically relevant biomarkers for seizure and artifact detection. This suggests that for biomedical time-series, “faithful” reconstruction of the raw signal is suboptimal; instead, reconstruction targets should be aligned with the physiological bandwidth of interest.

B. The Quantization-Efficiency Trade-off

The successful compression of FEMBA to 2-bit weights (W2A8) without performance collapse is a key finding. Prior work on Mamba has highlighted the difficulty of PTQ due to activation outliers in the selective scan [30]. Our experiments confirm this: PTQ failed catastrophically (AUROC ≈ 0.5). However, QAT allowed the model to adapt its weights to the low-precision regime. Interestingly, while 2-bit quantization reduced the memory footprint by 74% (enabling deployment on the 1.5MB L2 memory of GAP9), it did not significantly reduce latency. This confirms that our implementation is *compute-bound*, not memory-bound. The implications are two-fold: (1) aggressive quantization is essential for *storage* on MCUs, but (2) accelerating inference requires dedicated hardware support for the SSM scan operations, rather than just memory bandwidth reduction.

C. Limitations and Future Work

While FEMBA demonstrates robust performance across several adult EEG datasets, important limitations exist. First, our pre-training and evaluation are confined to the TUEG, TUAB, TUAR, and TUSL corpora, which primarily comprise clinical adult recordings from related acquisition pipelines. Generalization to substantially different domains—such as neonatal EEG with burst-suppression patterns, high-density research montages, consumer headsets with few dry electrodes, or home-based long-term monitoring—remains unestablished. Extending the pre-training to more diverse data sources and explicitly quantifying out-of-distribution robustness will be crucial.

Second, the current deployment operates on fixed, non-overlapping 5s windows and performs offline classification. Many clinical and consumer applications, however, require streaming or event-triggered processing with strict low-latency constraints. Adapting FEMBA to a fully streaming inference regime—e.g., by exploiting causal variants of the state-space recurrence and reusing internal states across windows—could reduce latency and energy further, but may require retraining and task-specific calibration.

TABLE IX: Sub-operation Breakdown for mamba_blocks.0

Operation	Cycles (M)	%	MACs (M)	MACs/Cyc
Input Projection	71.7	23.2%	189.7	2.65
Sequence Reversal	1.6	0.5%	—	—
Local Temporal Conv.	8.8	2.8%	1.0	0.11
Selective SSM Scan	199.5	64.6%	63.1	0.32
Output Projection	24.3	7.9%	94.9	3.91
Sequence Reversal	1.0	0.3%	—	—
Bidirectional Fusion	2.1	0.7%	—	—
Total	308.9	100%	348.7	1.13

Third, our quantization scheme is validated primarily on the FEMBA-Tiny architecture and TUAB-based downstream tasks. Although the W2A8 configuration with a small number of higher-precision accumulators proved sufficient in this setting, different hyperparameters, model scales, or target MCUs may exhibit different sensitivity to quantization noise. Systematically exploring mixed-precision assignments and automatically tuning quantization parameters for new hardware platforms is, therefore, an open direction.

Fourth, this study focuses on algorithmic and embedded feasibility rather than clinical workflow integration. All evaluations are performed on retrospective datasets; we do not assess prospective performance, user comfort, or the impact of FEMBA-based alerts on clinical decision-making. Future work must investigate how such models affect false-alarm rates, time-to-detection, and interpretability in real-world monitoring scenarios, ideally with clinical partners.

Finally, our hardware analysis highlights a fundamental architectural bottleneck: the selective SSM scan achieves only about 0.32 MACs/cycle on the GAP9 cluster due to its inherently sequential nature and limited instruction-level parallelism, whereas dense linear projections can reach up to 3.9 MACs/cycle. Recent formulations such as Mamba-2, which recast state-space recurrences into structured matrix multiplications, offer a promising path to replace this scan with matmul-friendly kernels that better exploit the GAP9 compute fabric. Given the strong efficiency of our linear layers, integrating such “matmul-friendly” SSM variants is a natural avenue to further accelerate edge inference in future versions of FEMBA.

VI. CONCLUSION

This work bridges the gap between large-scale Foundation Models and the resource constraints of wearable biomedical devices. We introduced FEMBA, a bidirectional Mamba architecture that leverages a novel Physiologically-Aware pre-training strategy to prioritize the reconstruction of neural oscillations over high-frequency artifacts. This approach yields superior generalization on diverse downstream tasks (TUAB, TUAR, TUSL) compared to standard masked modeling.

Furthermore, we addressed the critical challenge of deploying State-Space Models on MCUs. By utilizing QAT, we overcame the activation outlier issue inherent to Mamba, successfully compressing the model to 2-bit weights with negligible performance degradation. The resulting deployment on a parallel RISC-V MCU (GAP9) achieves deterministic real-time inference (1.70 s per window) with a 74% reduction in memory footprint.

These results demonstrate that the linear complexity of SSMs, combined with quantization, makes them a viable alternative to Transformer-based models for ambulatory neuro-monitoring. By enabling high-performance artifact and seizure detection directly at the edge, FEMBA paves the way for energy-efficient, long-term wearable health systems that do not rely on continuous cloud connectivity. Future work will focus on architectural approximations to further parallelize the selective scan mechanism, unlocking the full throughput potential of embedded parallel clusters.

REFERENCES

- [1] T. F. Collura, “History and evolution of electroencephalographic instruments and techniques,” *Journal of clinical neurophysiology*, vol. 10, no. 4, pp. 476–504, 1993.
- [2] D. Petit, J.-F. Gagnon, M. L. Fantini, L. Ferini-Strambi, and J. Montplaisir, “Sleep and quantitative eeg in neurodegenerative disorders,” *Journal of psychosomatic research*, vol. 56, no. 5, pp. 487–496, 2004.
- [3] S. Noachtar and J. Rémi, “The role of eeg in epilepsy: a critical review,” *Epilepsy & Behavior*, vol. 15, no. 1, pp. 22–33, 2009.
- [4] S. Beniczky, S. Wiebe, J. Jeppesen, W. O. Tatum, M. Brazdil, Y. Wang, S. T. Herman, and P. Ryvlin, “Automated seizure detection using wearable devices: a clinical practice guideline of the international league against epilepsy and the international federation of clinical neurophysiology,” *Clinical Neurophysiology*, vol. 132, no. 5, pp. 1173–1184, 2021.
- [5] R. L. Acabchuk, M. A. Simon, S. Low, J. M. Brisson, and B. T. Johnson, “Measuring meditation progress with a consumer-grade eeg device: Caution from a randomized controlled trial,” *Mindfulness*, vol. 12, no. 1, pp. 68–81, 2021.
- [6] L.-D. Liao, C.-Y. Chen, I.-J. Wang, S.-F. Chen, S.-Y. Li, B.-W. Chen, J.-Y. Chang, and C.-T. Lin, “Gaming control using a wearable and wireless eeg-based brain-computer interface device with novel dry foam-based sensors,” *Journal of neuroengineering and rehabilitation*, vol. 9, no. 1, p. 5, 2012.
- [7] A. Ahmadi, O. Dehzangi, and R. Jafari, “Brain-computer interface signal processing algorithms: A computational cost vs. accuracy analysis for wearable computers,” in *2012 Ninth International Conference on Wearable and Implantable Body Sensor Networks*. IEEE, 2012, pp. 40–45.
- [8] D. Seok, S. Lee, M. Kim, J. Cho, and C. Kim, “Motion artifact removal techniques for wearable eeg and ppg sensor systems,” *Frontiers in Electronics*, vol. 2, p. 685513, 2021.
- [9] T. M. Ingolfsson, S. Benatti, X. Wang, A. Bernini, P. Ducouret, P. Ryvlin, S. Beniczky, L. Benini, and A. Cossetti, “Minimizing artifact-induced false-alarms for seizure detection in wearable EEG devices with gradient-boosted tree classifiers,” *Sci Rep*, vol. 14, no. 1, p. 2980, Feb. 2024.
- [10] F. Lotte, M. Congedo, A. Lécuyer, F. Lamarche, and B. Arnaldi, “A review of classification algorithms for eeg-based brain-computer interfaces,” *Journal of neural engineering*, vol. 4, no. 2, p. R1, 2007.
- [11] T. M. Ingolfsson, M. Hersche, X. Wang, N. Kobayashi, L. Cavigelli, and L. Benini, “EEG-TCNet: An accurate temporal convolutional network for embedded motor-imagery brain-machine interfaces,” in *2020 IEEE International Conference on Systems, Man, and Cybernetics (SMC)*, 2020, pp. 2958–2965.
- [12] R. Zanetti, A. Arza, A. Aminifar, and D. Aienza, “Real-time eeg-based cognitive workload monitoring on wearable devices,” *IEEE transactions on biomedical engineering*, vol. 69, no. 1, pp. 265–277, 2021.
- [13] T. M. Ingolfsson, X. Wang, U. Chakraborty, S. Benatti, A. Bernini, P. Ducouret, P. Ryvlin, S. Beniczky, L. Benini, and A. Cossetti, “BrainFuseNet: Enhancing Wearable Seizure Detection Through EEG-PPG-Accelerometer Sensor Fusion and Efficient Edge Deployment,” *IEEE Transactions on Biomedical Circuits and Systems*, vol. 18, no. 4, pp. 720–733, Aug. 2024.
- [14] S. Frey, M. A. Lucchini, V. Kartsch, T. M. Ingolfsson, A. H. Bernardi, M. Segessenmann, J. Osielec, S. Benatti, L. Benini, and A. Cossetti, “Gapses: Versatile smart glasses for comfortable and fully-dry acquisition and parallel ultra-low-power processing of eeg and eog,” *IEEE Transactions on Biomedical Circuits and Systems*, 2024.
- [15] D. Kostas, S. Aroca-Ouellette, and F. Rudzicz, “Bendr: Using transformers and a contrastive self-supervised learning task to learn from massive amounts of EEG data,” *Frontiers in Human Neuroscience*, vol. 15, p. 653659, 2021.
- [16] W. Jiang, L. Zhao, and B. liang Lu, “Large brain model for learning generic representations with tremendous EEG data in BCI,” in *The Twelfth International Conference on Learning Representations*, 2024.
- [17] J. Wang, S. Zhao, Z. Luo, Y. Zhou, H. Jiang, S. Li, T. Li, and G. Pan, “CBramod: A criss-cross brain foundation model for EEG decoding,” in *The Thirteenth International Conference on Learning Representations*, 2025.
- [18] A. Gu and T. Dao, “Mamba: Linear-time sequence modeling with selective state spaces,” in *First conference on language modeling*, 2024.
- [19] A. Tegov, T. M. Ingolfsson, X. Wang, L. Benini, and Y. Li, “Femba: Efficient and scalable eeg analysis with a bidirectional mamba foundation model,” in *2025 47th Annual International Conference of the IEEE Engineering in Medicine and Biology Society (EMBC)*, 2025, pp. 1–7.

- [20] R. T. Schirmer, J. T. Springenberg, L. D. J. Fiederer, M. Glasstetter, K. Eggensperger, M. Tangermann, F. Hutter, W. Burgard, and T. Ball, "Deep learning with convolutional neural networks for eeg decoding and visualization," *Human brain mapping*, vol. 38, no. 11, pp. 5391–5420, 2017.
- [21] V. J. Lawhern, A. J. Solon, N. R. Waytowich, S. M. Gordon, C. P. Hung, and B. J. Lance, "EEGNet: a compact convolutional neural network for EEG-based brain-computer interfaces," *Journal of neural engineering*, vol. 15, no. 5, p. 056013, 2018.
- [22] G. A. Altuwajri and G. Muhammad, "A multibranch of convolutional neural network models for electroencephalogram-based motor imagery classification," *Biosensors*, vol. 12, no. 1, p. 22, 2022.
- [23] D. Kostas and F. Rudzicz, "Thinker invariance: enabling deep neural networks for BCI across more people," *Journal of Neural Engineering*, vol. 17, no. 5, p. 056008, 2020.
- [24] S. Kumar, A. Sharma, and T. Tsunoda, "Brain wave classification using long short-term memory network based optical predictor," *Scientific reports*, vol. 9, no. 1, p. 9153, 2019.
- [25] T.-j. Luo, C.-l. Zhou, and F. Chao, "Exploring spatial-frequency-sequential relationships for motor imagery classification with recurrent neural network," *BMC bioinformatics*, vol. 19, no. 1, p. 344, 2018.
- [26] C. Wang, V. Subramaniam, A. U. Yaari, G. Kreiman, B. Katz, I. Cases, and A. Barbu, "BrainBERT: Self-supervised representation learning for intracranial recordings," in *The Eleventh International Conference on Learning Representations*, 2023.
- [27] Y. Gui, M. Chen, Y. Su, G. Luo, and Y. Yang, "EEGMamba: Bidirectional state space model with mixture of experts for EEG multi-task classification," *arXiv preprint arXiv:2407.20254*, 2024.
- [28] J. Hong, G. Mackellar, and S. Ghane, "Eegm2: An efficient mamba-2-based self-supervised framework for long-sequence EEG modeling," *arXiv preprint arXiv:2502.17873*, 2025.
- [29] T. M. Ingolfsson, X. Wang, M. Hersche, A. Burrello, L. Cavigelli, and L. Benini, "Ecg-tcn: Wearable cardiac arrhythmia detection with a temporal convolutional network," in *2021 IEEE 3rd International Conference on Artificial Intelligence Circuits and Systems (AICAS)*, 2021, pp. 1–4.
- [30] Z. Xu, Y. Yue, X. Hu, D. Yang, Z. Yuan, Z. Jiang, Z. Chen, JiangyongYu, XUCHEN, and S. Zhou, "Mambaquant: Quantizing the mamba family with variance aligned rotation methods," in *The Thirteenth International Conference on Learning Representations*, 2025.
- [31] I. Obeid and J. Picone, "The Temple University Hospital EEG Data Corpus," *Frontiers in Neuroscience*, vol. 10, May 2016.
- [32] M. Bedeuzzaman, O. Farooq, and Y. U. Khan, "Automatic seizure detection using inter quartile range," *Int. Journal of Computer Applications*, vol. 44, no. 11, pp. 1–5, 2012.
- [33] O. Lieber, B. Lenz, H. Bata, G. Cohen, J. Osin, I. Dalmedigos, E. Safahi, S. Meiroum, Y. Belinkov, S. Shalev-Shwartz *et al.*, "Jamba: A hybrid transformer-mamba language model," *arXiv preprint arXiv:2403.19887*, 2024.
- [34] R. Girshick, "Fast R-CNN ICCV," in *Proc. of the IEEE Int. Conf. on Computer Vision (ICCV)*, 2015, pp. 1440–1448.
- [35] P. Arpaia, M. De Luca, L. Di Marino, D. Duran, L. Gargiulo, P. Lanteri, N. Moccaldi, M. Nalin, M. Picciafuoco, R. Robbio *et al.*, "A systematic review of techniques for artifact detection and artifact category identification in electroencephalography from wearable devices," *Sensors*, vol. 25, no. 18, p. 5770, 2025.
- [36] L. Yang and S. Hong, "Unsupervised time-series representation learning with iterative bilinear temporal-spectral fusion," in *International conference on machine learning*. PMLR, 2022, pp. 25 038–25 054.
- [37] A. v. d. Oord, Y. Li, and O. Vinyals, "Representation learning with contrastive predictive coding," *arXiv preprint arXiv:1807.03748*, 2018.
- [38] C. Rommel, J. Paillard, T. Moreau, and A. Gramfort, "Data augmentation for learning predictive models on EEG: a systematic comparison," *Journal of Neural Engineering*, vol. 19, no. 6, p. 066020, 2022.
- [39] J. T. Schwabedal, J. C. Snyder, A. Cakmak, S. Nemati, and G. D. Clifford, "Addressing class imbalance in classification problems of noisy signals by using Fourier transform surrogates," *arXiv preprint arXiv:1806.08675*, 2018.
- [40] C. Rommel, T. Moreau, J. Paillard, and A. Gramfort, "CADDA: Class-wise automatic differentiable data augmentation for EEG signals," in *International Conference on Learning Representations*, 2022.
- [41] O. Yonay, T. Hammond, and T. Yang, "Myna: Masking-based contrastive learning of musical representations," *arXiv preprint arXiv:2502.12511*, 2025.
- [42] Y. Chen, K. Ren, K. Song, Y. Wang, Y. Wang, D. Li, and L. Qiu, "EEGFormer: Towards transferable and interpretable large-scale EEG foundation model," in *AAAI 2024 Spring Symposium on Clinical Foundation Models*, 2024.
- [43] T.-Y. Lin, P. Goyal, R. Girshick, K. He, and P. Dollár, "Focal loss for dense object detection," in *Proceedings of the IEEE international conference on computer vision*, 2017, pp. 2980–2988.
- [44] G. Franco, A. Pappalardo, and N. J. Fraser, "Xilinx/brevitas," 2025. [Online]. Available: <https://doi.org/10.5281/zenodo.3333552>
- [45] B. Rokh, A. Azarpeyvand, and A. Khanteymoori, "A comprehensive survey on model quantization for deep neural networks in image classification," *ACM Transactions on Intelligent Systems and Technology*, vol. 14, no. 6, pp. 1–50, 2023.
- [46] GreenWaves Technologies, "GAP SDK: Sdk for greenwaves technologies' gap8 iot application processor," https://github.com/GreenWavesTechnologies/gap_sdk, 2022, version 4.12.0.
- [47] F. Daghero, D. J. Pagliari, F. Conti, L. Benini, M. Poncino, and A. Burrello, "Lightweight software kernels and hardware extensions for efficient sparse deep neural networks on microcontrollers," in *Eighth Conference on Machine Learning and Systems*, 2025.
- [48] A. Garofalo, M. Rusci, F. Conti, D. Rossi, and L. Benini, "Pulp-nn: Accelerating quantized neural networks on parallel ultra-low-power risc-v processors," *Philosophical Transactions of the Royal Society A*, vol. 378, no. 2164, p. 20190155, 2020.
- [49] B. Döner, T. M. Ingolfsson, L. Benini, and Y. Li, "LUNA: Efficient and topology-agnostic foundation model for EEG signal analysis," in *The Thirty-ninth Annual Conference on Neural Information Processing Systems*, 2025.
- [50] A. Demir, T. Koike-Akino, Y. Wang, M. Haruna, and D. Erdogmus, "EEG-GNN: Graph neural networks for classification of electroencephalogram (EEG) signals," in *2021 43rd Annual International Conference of the IEEE Engineering in Medicine & Biology Society (EMBC)*. IEEE, 2021, pp. 1061–1067.
- [51] S. Tang, J. A. Dunmon, Q. Liangqiong, K. K. Saab, T. Baykaner, C. Lee-Messer, and D. L. Rubin, "Modeling multivariate biosignals with graph neural networks and structured state space models," in *Conference on health, inference, and learning*. PMLR, 2023, pp. 50–71.
- [52] J. Jing, W. Ge, S. Hong, M. B. Fernandes, Z. Lin, C. Yang, S. An, A. F. Struck, A. Herlopian, I. Karakis *et al.*, "Development of expert-level classification of seizures and rhythmic and periodic patterns during EEG interpretation," *Neurology*, vol. 100, no. 17, pp. e1750–e1762, 2023.
- [53] C. Yang, C. Xiao, M. B. Westover, and J. Sun, "Self-supervised electroencephalogram representation learning for automatic sleep staging: model development and evaluation study," *JMIR AI*, vol. 2, no. 1, p. e46769, 2023.
- [54] W. Y. Peh, Y. Yao, and J. Dauwels, "Transformer convolutional neural networks for automated artifact detection in scalp EEG," in *2022 44th Annual International Conference of the IEEE Engineering in Medicine & Biology Society (EMBC)*. IEEE, 2022, pp. 3599–3602.
- [55] H. Li, M. Ding, R. Zhang, and C. Xiu, "Motor imagery EEG classification algorithm based on CNN-LSTM feature fusion network," *Biomedical signal processing and control*, vol. 72, p. 103342, 2022.
- [56] Y. Song, X. Jia, L. Yang, and L. Xie, "Transformer-based spatial-temporal feature learning for EEG decoding," *arXiv preprint arXiv:2106.11170*, 2021.
- [57] C. Yang, M. Westover, and J. Sun, "Biot: Biosignal transformer for cross-data learning in the wild," *Advances in Neural Information Processing Systems*, vol. 36, pp. 78 240–78 260, 2023.
- [58] N. Mohammadi Foumani, G. Mackellar, S. Ghane, S. Irtza, N. Nguyen, and M. Salehi, "Eeg2rep: enhancing self-supervised EEG representation through informative masked inputs," in *Proceedings of the 30th ACM SIGKDD Conference on Knowledge Discovery and Data Mining*, 2024, pp. 5544–5555.
- [59] A. Dimofte, G. A. Bucagu, T. M. Ingolfsson, X. Wang, A. Cossetini, L. Benini, and Y. Li, "CEReBrO: Compact encoder for representations of brain oscillations using efficient alternating attention," *arXiv preprint arXiv:2501.10885*, 2025.
- [60] N. Lee, K. Barmpas, A. Kolioussis, Y. Panagakis, D. Adamos, N. Laskaris, and S. Zafeiriou, "A comprehensive review of biosignal foundation models," *Authorea Preprints*, 2025.
- [61] G. Rutishauser, J. Mihali, M. Scherer, and L. Benini, "xtern: Energy-efficient ternary neural network inference on risc-v-based edge systems," in *2024 IEEE 35th International Conference on Application-specific Systems, Architectures and Processors (ASAP)*. IEEE, 2024, pp. 206–213.
- [62] I. I. Goncharova, D. J. McFarland, T. M. Vaughan, and J. R. Wolpaw, "Emg contamination of eeg: spectral and topographical characteristics," *Clinical neurophysiology*, vol. 114, no. 9, pp. 1580–1593, 2003.